AGU PUBLICATIONS

Geochemistry, Geophysics, Geosystems

RESEARCH ARTICLE
10.1002/2017GC007280

Derivation and Error Analysis of the Earth Magnetic Anomaly Grid at 2 arc min Resolution Version 3 (EMAG2v3)

B. Meyer[1], A. Chulliat[1], and R. Saltus[1]

[1]Boulder CIRES and NOAA NCEI, University of Colorado, Boulder, CO, USA

Key Points:
- This grid combines marine, airborne, ground, and satellite observations to map magnetic anomalies arising from lithospheric sources
- The grid was compiled using no a priori information about geologic structures or ages
- It includes over 50 million new data points added to the Geophysical Database System (GEODAS) in recent years

Supporting Information:
- Supporting Information S1
- Data Set S1

Correspondence to:
B. Meyer,
brian.meyer@noaa.gov

Citation:
Meyer, B., Chulliat, A., & Saltus, R. (2017). Derivation and error analysis of the earth magnetic anomaly grid at 2 arc min resolution version 3 (EMAG2v3). *Geochemistry, Geophysics, Geosystems*, *18*, 4522–4537. https://doi.org/10.1002/2017GC007280

Received 6 OCT 2017
Accepted 27 NOV 2017
Accepted article online 30 NOV 2017
Published online 19 DEC 2017

Abstract The Earth Magnetic Anomaly Grid at 2 arc min resolution version 3, EMAG2v3, combines marine and airborne trackline observations, satellite data, and magnetic observatory data to map the location, intensity, and extent of lithospheric magnetic anomalies. EMAG2v3 includes over 50 million new data points added to NCEI's Geophysical Database System (GEODAS) in recent years. The new grid relies only on observed data, and does not utilize a priori geologic structure or ocean-age information. Comparing this grid to other global magnetic anomaly compilations (e.g., EMAG2 and WDMAM), we can see that the inclusion of a priori ocean-age patterns forces an artificial linear pattern to the grid; the data-only approach allows for greater complexity in representing the evolution along oceanic spreading ridges and continental margins. EMAG2v3 also makes use of the satellite-derived lithospheric field model MF7 in order to accurately represent anomalies with wavelengths greater than 300 km and to create smooth grid merging boundaries. The heterogeneous distribution of errors in the observations used in compiling the EMAG2v3 was explored, and is reported in the final distributed grid. This grid is delivered at both 4 km continuous altitude above WGS84, as well as at sea level for all oceanic and coastal regions.

Plain Language Summary Rocks and minerals have differing magnetic properties that can enhance or suppress the local magnetic field, whose primary source is the Earth's core. These fluctuations, called magnetic anomalies, can be up to 10% of the strength of the total field. Analysis and interpretation of magnetic anomalies is used in geodynamic, tectonic, and geological investigations, as well as in geophysical exploration; these anomalies can also significantly distort local compass and GPS headings. EMAG2v3 provides a global map of the location and strength of these anomalies that can be used to increase navigational accuracy and to study the structure and evolution of the Earth's lithosphere. It comes with a global map of uncertainties, reflecting heterogeneity in survey data quality.

1. Introduction

Global magnetic anomaly maps derived from marine, airborne, and satellite measurements have only relatively recently become available. Although magnetic anomaly maps have long been an essential tool for investigating the structure and evolution of the Earth's lithosphere and for mineral resource exploration, such maps typically cover ad hoc areas determined by specific survey goals. Composite maps covering larger areas, such as an entire country or continent (e.g., Hinze & Zietz, 1985), were often built; however, they lacked meaningful information on large-scale magnetic anomalies. The situation changed in the 2000s (e.g., Saltus, 2007) when high quality, low-Earth orbit magnetic measurements by the CHAMP satellite (Reigber et al., 2002) became available and allowed for the calculation of global spherical harmonic models of the lithospheric field down to about 330 km spatial resolution (Maus et al., 2007a, 2008). This, together with increasing international cooperation under the auspices of the International Association of Geomagnetism and Aeronomy (IAGA) and the Commission for the Geological Map of the World (CGMW), led to the development of the first World Digital Magnetic Anomaly Map (WDMAM, Korhonen et al., 2007), a 3 arc min resolution grid at an altitude of 5 km above the WGS84 reference ellipsoid based on candidate grids from various groups (e.g., Hamoudi et al., 2007; Maus et al., 2007b). Soon after, Maus et al. (2009) developed the 2 arc min resolution Earth Magnetic Anomaly Grid (EMAG2), a new grid with more data, an improved spatial resolution and a reduced altitude of 4 km.

EMAG2 has been widely used since its release. The vast majority of papers citing the EMAG2 paper (Maus et al., 2009) are tectonic, geodynamic, and geological studies focusing on a particular area of the world and using EMAG2 as a reference map for the regional lithospheric magnetic field. These studies deal with a large

variety of geological settings, including continental fault zones (e.g., Webb et al., 2010), continental margins (e.g., Williams et al., 2011), and mid-ocean ridges (e.g., Schlindwein & Schmid, 2016). Some studies involve regional (e.g., Vérard et al., 2012) or global (Seton et al., 2012) geodynamic reconstructions of plate systems, or are motivated by applications, such as oil exploration (e.g., Dickson et al., 2016). EMAG2 was also used as a reference map for new aeromagnetic surveys (Matzka et al., 2010) and ocean drilling studies (Jaeger et al., 2014). Outside the realm of geology, EMAG2 was used in research on geomagnetism-based navigation techniques (Claus & Bachmayer, 2017; Zheng et al., 2013). To facilitate data visualization and analysis, EMAG2 was incorporated in Google Earth, NASA World Wind and other virtual globes (Müller et al., 2016).

The high-resolution, ellipsoidal harmonic model of the Earth's lithospheric field developed by Maus (2010) is an important product derived from EMAG2. While EMAG2 (and similar grids) only provide the scalar total field anomaly, spherical or ellipsoidal harmonic models provide the three vector components of the lithospheric field at any location near the Earth's surface. This information, when combined with a main field model, can be used for navigation (cf. NOAA's Enhanced Magnetic Model, https://www.ngdc.noaa.gov/geomag/EMM) and applications, such as directional drilling (Maus et al., 2012).

This paper presents a new global, 2 arc min resolution magnetic anomaly grid, developed using a different method than EMAG2 and a fully independent processing sequence. It includes over 50 million new data points, mostly over marine areas, which were added to NCEI's Geophysical Database System (GEODAS) since 2009. This new grid is named EMAG2v3 ("version 3"), to distinguish it from NOAA's previous 2 arc min resolution grid, EMAG2, which was referred to as EMAG2 "version 2" within NOAA's National Centers for Environmental Information (NCEI, formerly NGDC).

In both EMAG2 and the first WDMAM, some a priori information was used to fill some or all of the data gaps in oceanic areas. Unfortunately, these gaps are particularly wide in the Southern Hemisphere. In EMAG2, a directional gridding algorithm was used, with larger correlation lengths along isochrons as given by an oceanic crustal age model (Müller et al., 2008). In the first WDMAM, gaps were directly filled with synthetic magnetic anomalies derived from an oceanic crustal age model. This process of filling data gaps was done for visualization purposes only, and not an attempt to predict anomaly intensity or structure in nonsurveyed areas. Recently, a second version of the WDMAM was released (Lesur et al., 2016), with the same resolution and altitude as the original one, but a revised method to handle marine data sets. In this latter grid, a forward model of marine magnetic anomalies was built from an age map of the ocean floor, relative plate motions, and a geomagnetic polarity time scale, then adjusted to marine data and finally calculated over all oceanic areas (Dyment et al., 2015). Such sophisticated approaches obviously have great merits, such as significantly reducing the size of data gaps and, in the case of the second WDMAM, providing a global equivalent magnetization map covering the entire oceanic lithosphere. However, they run the risk of attributing too much weight to a priori information in areas well covered by observed data, and could mislead users about the quality and quantity of data coverage. For these reasons, it was decided that no a priori information would be used to fill data gaps in EMAG2v3.

Other differences between EMAG2v3 and EMAG2 include: (a) removing a number of outliers in marine and airborne trackline data, thanks to an improved data preprocessing scheme; (b) substituting long-wavelength anomalies with the more recent and higher resolution MF7 satellite-based lithospheric field model (available at https://geomag.colorado.edu/magnetic-field-model-mf7.html and derived with a method similar to MF6, Maus et al., 2008); (c) using a new precompiled grid for Alaska; (d) estimating errors for each continental subgrid; (e) subdividing oceanic areas in 21 tiles and estimating EMAG2v3 errors for each tile. Finally, special attention was paid to designing a workflow such that frequent updates would be possible in the future, for example, when new data become available.

In what follows, we first present the various data sets used in EMAG2v3 and the data processing steps (section 2). We then report on the error analysis, both for continental and oceanic areas (section 3). In section 4, the final grid is presented, discussed and compared to EMAG2 and the most recent WDMAM.

2. Data Sets and Processing

2.1. Source Grid Design

The primary data sources for the compilation of global magnetic anomalies are marine and airborne trackline geophysical surveys. These surveys have been provided to NCEI, the World Data Center for these types

Table 1
List of Geographical Tiles Used in Processing Marine Trackline Data, and of Filtered Trackline Intersection Statistics for Each Marine Tile

Tile	Total error (nT)	Mean (nT) bias	STD (nT) precision
Mediterranean	41	30.6	27.4
Central Atlantic	54	37	38.7
Indian Ocean	56	38.5	41.1
North Atlantic 3	61	36	49.7
Caribbean/Gulf of Mexico	63	44.3	45.3
North Atlantic 1	65	43.1	48.5
Baja California/Eastern Pacific	80	52.4	60.9
Arabian Ocean Airborne	84	61.5	57.6
Tierra del Fuego/South East Pacific	91	60.6	67.9
Tasmania/South Australia	92	62.6	67.9
South East Pacific	100	66.1	75.7
Cape of Good Hope/South East Atlantic	106	75.4	74.3
North Atlantic 2	107	73.5	77.8
Arabian Ocean Shipborne	110	58.5	92.7
Southern Ocean	113	79.1	80.8
North Atlantic 4	123	84.1	89.1
North Atlantic 5	124	69.1	103.5
North West Pacific	128	85.4	94.7
South Pacific	146	99.3	107.5
South West Atlantic	151	98.5	114.5
North Pacific	165	107	125.7
Mean of all Tiles	98	65	73

of data, by greater than 100 institutions and collected over the past 50 years. Since the release of EMAG2 (Maus et al., 2009), there has been a concerted effort to increase the volume and value of the data within the NOAA archive, known as Geophysical Data System (GEODAS), as well as to modernize data discovery, availability, and delivery to the public.

This data holding has increased by adding 657 individual surveys (25% increase), which consist of 50.6 million data points (200%) over 2.5 million miles (31%) since 2009. The entire database consists of 3,255 surveys, 76.1 million data points covering 10.5 million trackline miles. Much of the data recently ingested into GEODAS has been collected at a high sampling rate, with more accurate magnetometers and navigation systems. The design of the data discovery interface has moved from a FORTRAN, text based user interface to a GIS interactive map based interface. This has made the data retrieval process more modern, intuitive, and robust, providing users with more data options and customizability.

In order to deal with the large volume of data, as well as the heterogeneity in data distribution, the oceanic regions were split into 21 individual tiles (see the list in Table 1). These tiles were selected by creating rectangular bounding boxes which encompass a relatively homogeneous distribution of data, a consistent tectonic structure (relatively persistent direction of spreading ridge anomalies), and a total number of data observations that allows for computational efficiency. To encourage smooth transitions between the gridded marine tiles, each tile overlaps its neighboring tiles by 1°. The airborne data were extended 5° beyond the boundary to aid in the tile merging process, and to avoid edge effects that may result from the gridding process.

For the majority of the continental regions, NCEI does not have the raw aeromagnetic data available. In the few instances that we do, we trust that the producers of the regional grids have more time and expertise in the regions to produce the best possible grids for the area. These grids were provided to NCEI by academic institutions, government agencies, and industry from around the world (Table 2).

Most continental grids used in EMAG2v3 were also used in EMAG2. The exceptions are that we used a new regional magnetic anomaly grid of Alaska, provided by Richard Saltus, which was upward continued and properly sampled to be analogous with the existing grids, as well as the newer release of the Magnetic Anomaly Map of North America developed by the North American Magnetic Anomaly Group (NAMAG, 2002) and distributed by the US Geological Survey. As we become aware of new updated grids, we will incorporate them into future updates.

2.2. Continental Grid Processing

All continental grids used in the completion of EMAG2v3 were upward continued to 4 km and sampled at 2 arc min resolution, as described in Maus et al. (2009).

The software Geosoft Oasis montaj provides robust capabilities in merging grids. Once the grids were imported into the proper format, they were then merged for each continent (i.e., North America, Europe, etc.), using MF7 as a long-wavelength trend to avoid edge effects. During this merging process, grids with higher energy were given priority. This is accomplished by setting the highest quality grids as the primary grids in the gridding queue so that the other grids will be leveled to and around in order of preference. Oasis montaj utilizes the long-wavelength grid to match intensities along border edges, creating a seamless merged final grid. During this gridding process, the grids are reinterpolated onto a uniform regular grid.

2.3. Trackline Data Selection and Processing

From the total NCEI data holdings only those trackline data that include full date, time, and total observed field were selected for inclusion in EMAG2v3. This selection is necessary so that main and external magnetic fields can be accurately removed from the measured values. There are surveys within the database that

Table 2
List of Contributing Pre-Compiled Continental Grids With Source Contributor, Altitude, Altitude Type (Barometric = Constant Altitude; Topographic = Variable aka "draped" Altitude), Resolution, Total Error, Mean, and Standard Deviation

Region	Source contributor	Altitude (m)	Altitude type	Resolution	Total error (nT)	MEAN (nT) bias	STD (nT) precision
Europe	Wonik et al. (2001)	3,000	Barometric	5 km	59	35	47
Northern hemisphere	Verhoef et al. (1996)	300	Topographic	5 km	100	62	78
Middle east	Mostly Iran	300	Topographic	5 km	231	135	188
East Asia	Coordinating Committee for Coastal and Offshore Geoscience Program in East and Southeast Asia (CCOP) compilation 2002	300	Topographic	5 km	217	127	175
Former Soviet Union	National Centers for Environmental Information (NOAA NCEI) archives	300	Topographic	5 km	95	57	77
India	Rajaram et al. (2006)	0	Topographic	50 km	178	106	143
Global	GETECH global data compilation	300	Topographic	15 min	116	70	93
France	Institut de Physique du Globe de Paris	3000	Barometric	10 km	189	112	153
Spain	Socias et al. (1991)	3000	Barometric	5 km	217	127	175
South Africa	South African Development Community (SADC) compilation	300	Topographic	5 km	155	93	124
Tanzania	National Centers for Environmental Information (NOAA NCEI) archives	100	Topographic	5 km	164	97	132
Fennoscandia	Geological Survey of Finland (GTK); Korhonen et al. (2007)	5,000	Barometric	5 km	96	58	77
Italy	Eni Italy	2,500	Barometric	5 km	176	104	142
Canary Islands	Instituto Geografico Nacional (IGN); Socias and Mezcua (1991)	3,200	Barometric	5 km	214	126	173
Argentinia offshore	Max *et al*., 1999	5,000	Barometric	5 km	214	126	173
Argentina onshore	Servicio Geologico Minero Argentino (SEGEMAR)	5,000	Barometric	5 km	214	126	173
Eurasia	National Centers for Environmental Information (NOAA NCEI) archives	300	Topographic	20 km	214	126	173
Russia	A.P. Karpinsky Russian Geological Research Institute (VSEGEI); Oleg Petrov and Tamara Litvinova	5,000	Barometric	20 km	214	126	173
India	National Centers for Environmental Information (NOAA NCEI) archives	2,000	Topographic	5 km	214	126	173
Australia	Geoscience Australia: Franklin et al. (2004)	100	Topographic	1 km	94	55	76
Alaska	Rick Saltus	300	Topographic	1 km	34	22	26
North America	North America Magnetic Anomaly Group: Bankey et al. (2002)	300	Topographic	1 km	32	20	25
Afghanistan	U.S. Geological Survey (USGS): Sweeney et al. (2007)	300	Topographic	5 km	187	110	151
Algeria	National Centers for Environmental Information (NOAA NCEI) archives	150	Topographic	5 km	239	139	194
Arctic, western portion	Gaina et al. (2011)	300	Topographic	5 km	37	24	28
Arctic, Russian portion	Gaina et al. (2011)	300	Topographic	20 km	95	57	77
Austria	Geological Survey of Austria (GBA); Robert Supper	5,000	Barometric	5 km	135	80	109
Bolivia	National Centers for Environmental Information (NOAA NCEI) archives	300	Topographic	5 km	214	126	173
East of Fiji	National Centers for Environmental Information (NOAA NCEI) archives	300	Barometric	5 km	214	126	173
Hawaii	U.S. Geological Survey (USGS)	100	Topographic	5 km	136	81	110
Ivory Coast	Canadian International Development Agency (CIDA)	100	Topographic	10 km	239	139	194
Japan	Nakatsuka et al. (2005)	4,500	Topographic	5 km	73	44	58
New Zealand	National Centers for Environmental Information (NOAA NCEI) archives	3,000	Barometric	10 km	214	126	173
Pacific (small area)	National Centers for Environmental Information (NOAA NCEI) archives	100	Topographic	5 km	214	126	173
Pakistan	Canadian International Development Agency (CIDA)	1,000	Topographic	10 km	238	139	194
				MEAN	158	93	127

only report residual field values, without reporting the total observed field value. Observed values could, in theory, be recalculated if the survey metadata contains sufficient information about the reference field model that was used to calculate the dF value, but this effort was not undertaken for this compilation. For trackline data, which have been collected over the course of 50 years, there is a high amount of variability in both the quality and sampling rates of the data sets, and for aeromagnetic surveys there is the variable collection altitude as well. The fact that the data format used by NCEI has been consistent since 1977 allows for efficient data processing and quality assurance.

Following data selection and initial quality control, crustal field anomalies $\boldsymbol{dF}$ were obtained at each time and location by removing the core field modulus $\boldsymbol{F_{core}}$ and (when available) the projection of the external field $\vec{\boldsymbol{B}}_{\boldsymbol{ext}}$ onto the core field $\vec{\boldsymbol{B}}_{\boldsymbol{core}}$ direction, from the measured scalar field $\boldsymbol{F_{measured}}$ (e.g., Langel & Hinze, 1998):

$$dF = F_{measured} - F_{core} - \frac{\vec{B}_{core}}{\|\vec{B}_{core}\|} \cdot \vec{B}_{ext}$$

This correction was achieved using various models, depending on the epoch. Data collected before 1962 were only corrected for the core field, using the International Geomagnetic Reference Field (IGRF, Thébault et al., 2015). Data collected during 1962–1999 were corrected for core and external fields using CM4 (Sabaka et al., 2004). Data collected from 2000 onward were corrected for the core field using CHAOS-5 (Finlay et al., 2015) and for external fields using CM4. During this process, each data point was assigned the relevant Kp index value and trackline surveys were further subdivided into linear segments, designated by a change in the line azimuth.

These lines were imported into a Geosoft Oasis montaj database to proceed with the remaining processing. Using the Grid Sample tool, each observed value location sampled the MF7 crustal field model (https://geomag.colorado.edu/magnetic-field-model-mf7.html and Maus et al., 2008). This was used to retrieve the long-wavelength component and a consistent baseline to level each line to. First, the first-order trend was removed from the calculated residual field along each line. Then the first-order trend of the MF7 values along each line was calculated and added to the detrended residual values. This accomplished a primary leveling of each line to MF7 and incorporated the long-wavelength trend to the data.

The majority of the trackline data are taken multiple kilometers away from the source material/seabed. This allows us to use gradients and total observed anomaly as a method to filter data spikes and poor quality surveys from the trackline data set. If the gradient between two subsequent points along a line was greater than 100 nT/km, or if the total calculated anomaly was greater than 1,000 nT, these points were discarded as noise. To avoid using data that may be contaminated by noise generated by geomagnetic storms, the Kp index value during the data collection had to be less than 6o.

For areas where the airborne data were completely covered by a continental grid (e.g., Afghanistan) or sufficiently covered by marine trackline observations (e.g., North Atlantic, tile 1) the airborne data were not used; otherwise the airborne data were used to fill gaps in the continental and marine data sets. The airborne magnetic trackline data were downward continued to sea level, using an average altitude of 4 km, and the data were merged into the marine trackline database. Any artifacts that were generated by 2-D downward continuation of airborne data were caught in the filtering process described above. An exception was made for the Arabian tile, where marine and airborne data were kept separate because the low density of the long-wavelength airborne data were diluting the high-energy anomalies provided by the marine data. In this case, the airborne data were gridded separately and used only to fill in gaps left by the marine data gridding process.

The data were gridded using a kriging process (e.g., Goovaerts, 1997), which was selected because it is able to handle data with high variability in data density and line azimuth. The Geosoft program has built in gridding capabilities, which were used for the generation of the marine tiles individually from the recalculated and filtered magnetic residual values. For each tile the default values in the Oasis Montaj kriging module were used, except for the interpolation distance. The maximum interpolation distance for the grids was set to be 0.8°. This allows a large window for the gridding process to incorporate a significant amount of data, and fill much of the grid space. This gridding process also utilizes a spherical semivariogram for each tile.

Line leveling, the systematic adjustment of trackline base levels based on roughly orthogonal line crossings, is commonly used in magnetic survey data processing. However, because of the large amount of data and the irregularity with which lines cross, line leveling improves some areas while worsening other areas; for this reason, line leveling was not performed. Instead the final data selection was done manually. As discussed below, we did calculate line crossing differences as part of our error evaluation.

A great benefit of using the Geosoft databases is the ability to trace a gridded anomaly value back to the data source. After an initial gridding of the filtered magnetic anomaly values, any irregular or suspicious anomaly values can easily be investigated. Some of these irregularities are line features from lines consistently shifted from the baseline, or circular features due to data spikes, that both fall beneath the filter threshold in total anomaly and gradient steepness so are not caught in the automatic data filtering. If one of these features follows or intersects a single trackline, then that line is removed and the grid is recreated. If the feature persists and is noted within other tracklines, then the anomaly was determined to be real.

2.4. Grid Merging

When merging the continental grids with the marine grids, the continental grids were given priority in the gridding queue. In areas with significant overlap between the two grids (primarily North America), the marine grids were clipped to the coastline in order to avoid loss of energy in the continental compilations due to the lower intensity of the oceanic grids.

Each grid was assigned a code so that every grid cell can be referenced to the primary source which contributed to its inclusion. This source code does not exclude any influence from other grids that may overlap that area, of which there may be several, but indicates the primary grid that provided the information to arrive at the given value. Continental grids were assigned numbers 1–38 and marine tiles were assigned 101–121.

Using these assigned grid codes, each EMAG2v3 cell was also assigned the corresponding calculated error as described in the following sections. Where no data are available, the grid code was assigned 999, the error was assigned to be −999 nT, and the anomaly value was designated as 99,999 nT.

In some instances, the edges between two or more grids were complicated and thus resulted in an ambiguous assignment of data source; this is especially prevalent in the Indian Ocean, where there is a complicated geometry between the Arabian tile marine data and the Arabian tile aeromagnetic data. To report this, these grid cells were assigned a source code of 888 and the error was assigned to be −888 nT.

The continental compilations were merged with 4 km upward continued versions of the marine tiles to produce a global, 2 arc min resolution grid at 4 km altitude. This grid was then inverted for a spherical harmonic field model to degree and order 300, using a method described in section 2.5.

The sea level marine tiles were merged with downward continued versions of the continental compilations to produce another global, 2 arc min resolution grid at 0 km altitude above WGS84. In this case, unlike for the grid at 4 km altitude, downward continuation of the continental grids is generally not stable because some continental sources are located above sea level. However, we proceeded with downward continuation in order to avoid edge effects of the coasts where shipborne data rarely goes all the way to the coast line, while often the continental data overlaps this region. The continental regions were then masked out to remove any confusion about the primary expected use of the grid, which is to evaluate magnetic anomalies in oceanic regions, primarily the deep oceans where observations are already multiple kilometers from the source.

2.5. Long-Wavelength Inversion

The same long-wavelength inversion method was applied to both the 4 km altitude and the sea level global anomaly grids obtained by merging marine tiles and continental subgrids. To begin with the grid was filtered using a Gaussian filter with a 25 arc min cutoff length and then subsampled onto a 10 arc min grid. Data gaps were then filled with MF7 values. The inverse problem was linearized by expressing each scalar anomaly as:

$$dF = \frac{\vec{B}_{core}}{||\vec{B}_{core}||} \cdot \vec{B}_{lith}$$

where $\vec{B}_{lith}$ is the vector lithospheric field, expressed as a spherical harmonic expansion to degree and order n. In both the MF7 filling and the inversion, the latest IGRF (Thébault et al., 2015) for epoch 2000 was

used as the core field. A simple regularization using the same weight for each degree and order was applied, to avoid an ill-conditioned normal matrix (e.g., Snieder & Trampert, 1999) and minimize the Backus effect (Backus, 1970; Stern & Bredekamp, 1975). The damping parameter was selected using the L-curve method. Finally, the damped least squares solution was obtained in only one iteration, using a Cholesky decomposition. A full description of the inversion method will be provided in a separate paper.

2.6. Grid Finalization

The MF7 lithospheric field model was used to substitute long wavelengths in the global grid with large-scale anomalies predicted by the satellite-based model. Specifically, the degree 300 model, produced by the long-wavelength inversion, was truncated at degree 145 using a polynomial filter for degrees larger than 134, removed from all global grid data, and MF7 generated values (to degree 133) were added to all grid data.

We finally checked that reinverting the corrected grid to degree and order 300 led to coefficients that match those of MF7 up to degree 133. The Mauersberger-Lowes power spectrum (Lowes, 1966) of differences between the obtained model and MF7 showed values smaller than 2 nT^2 for all degrees, and smaller than 1 nT^2 for most degrees lower than 50, to be compared with MF7 power values between 100 and 400 nT^2 for most degrees; absolute differences between individual coefficients were smaller than 0.1 nT for all but three coefficients.

The same procedure was used at 4 km altitude and at sea level, yielding the final grids shown in Figures 1 and 2. Both grids are available at https://www.ngdc.noaa.gov/geomag/emag2.html or https://doi.org/10.7289/V5H70CVX.

3. Error Analysis

We provide consistent mean and standard deviation error estimates for the 35 continental magnetic compilation grids that were used in the construction of the EMAG2v3. In these data sets, the crossover information is lost while gridding the data from original track line or land surveys. Hence, we employ a different method to assign errors.

We also recognize that a further source for error in reported anomaly value is the presumed static nature of the intensity and location of the anomalies. Thébault et al. (2009) found that the crustal field change for degrees 15–90 is about 0.06–0.12 nT/yr on average at the Earth's surface, with larger values in South America and a few other places, up to 1.3 nT/yr. This is below the errors listed in this paper, except possibly when considering very old (50+ years) grids in South America.

In this section, error is defined as the absolute value of the difference between the true crustal anomaly field of the Earth and the grid value at a given grid cell location, the mean error is the average error over the entire grid, and standard deviation is the calculated standard deviation for the error over the entire grid.

3.1. Continental Source Grid Error

3.1.1. Sources of Error

For the purpose of error estimation, we have subdivided the factors that contribute to errors in regional magnetic compilation grids into three general categories that relate to the steps in the process of collecting and merging these data.

1. Survey-specific error (SE).

   Survey-specific errors arise from the data collection, data processing, and construction of a data grid for an individual magnetic survey. We consider errors in: (a) navigation accuracy, *ne*; (b) correction for "diurnal" magnetic field variation during the survey, *de*; and (c) the overall geometry of the survey relative to the grid spacing, *ge*, to be the most important sources of survey-specific error.

   For survey-specific errors, we have used our personal experience and judgment to make estimates of the possible range of survey-specific mean and standard deviation of error for the best (SE_{best} = 0 nT mean and 1 nT standard deviation) and worst (SE_{worst} = 10 nT mean, 20 nT standard deviation) probable scenarios. These assumptions are documented within the accompanying spreadsheet supplement. Within this

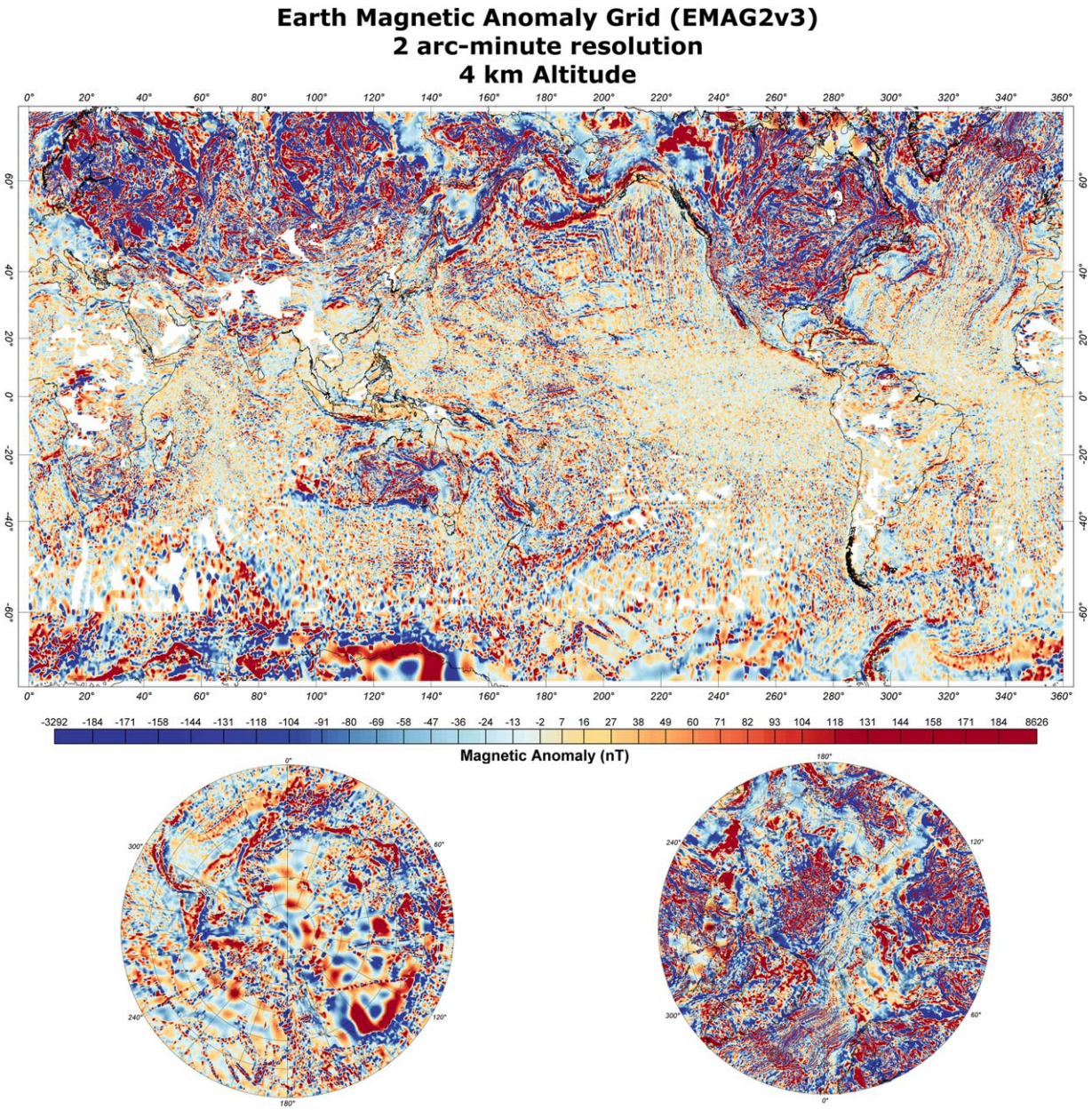

Figure 1. Earth Magnetic Anomaly Grid 2 arc min resolution Version 3 (EMAG2v3) at 4 km altitude. Global map (Mercator projection), North Polar and South Polar maps (polar stereographic projection).

best-to-worst range, we estimate the overall value for surveys used in the grid compilation using estimated quality factors ranging from 0 (worst case) to 1 (best case) for the three error sources (navigation = *qfn*, diurnal correction = *qfd*, survey geometry = *qfg*). The average of the quality factors and a "knowledge" factor (*k*, discussed below) is applied to select a value within the best-to-worst overall range.

So, in summary,

$$SE_{mean} = (SE_{worst} - (qfn * qfd * qfg * k) * (SE_{worst} - SE_{best}))_{mean}$$

$$SE_{std} = (SE_{worst} - (qfn * qfd * qfg * k) * (SE_{worst} - SE_{best}))_{std}$$

For example, for the Europe compilation grid in which generally good modern surveys were used and the procedures used are well documented (Wonik et al., 2001), we have assigned strong quality factors (*qfn* = 1,

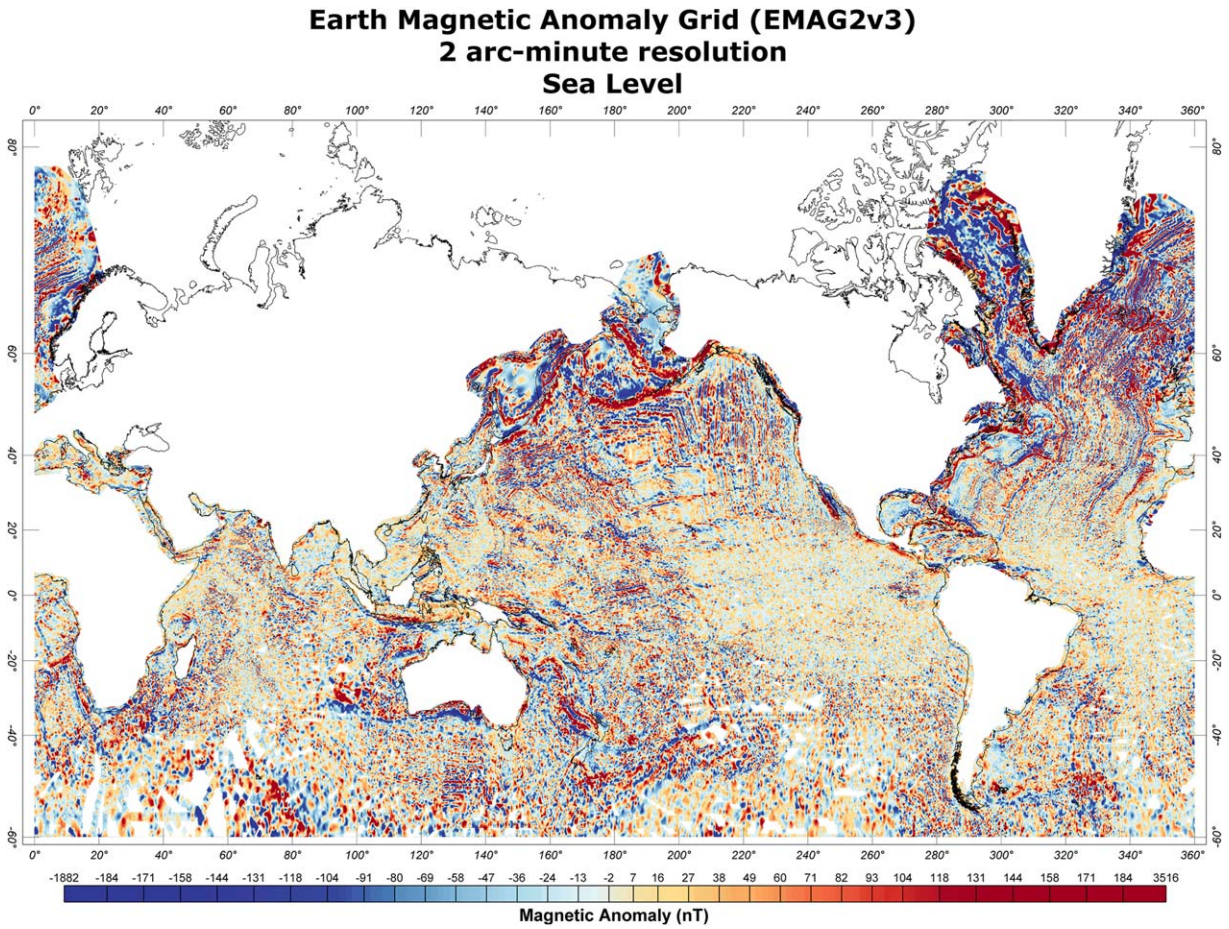

Figure 2. Earth Magnetic Anomaly Grid 2 arc min resolution Version 3 (EMAG2v3) at sea level (Mercator projection).

$qfd = 0.9$, and $qfg = 0.8$) and a 100% knowledge factor ($k = 1$). This gives a combined quality rating of 0.72 which yields $SE_{mean} = 3$ nT and $SE_{std} = 6$ nT.

1. Grid leveling (merging) error (GE).

   Data grids from individual surveys are merged together to create regional magnetic compilation grids. The resulting merged compilation grid will have errors related to uncertainties in the level-shifting and tilting generally employed in this process (e.g., Saltus, 2007). Modern compilations often use some independent information (e.g., MF7 or other similar models) to adjust grid levels during compilation.

   In a similar method to the error estimation for survey-specific error, we have defined best (10 nT mean, 20 nT standard deviation) and worst (50 nT mean, 100 nT standard deviation) case values for the mean and standard deviation of this error and use a single 0–1 quality factor estimate, *qfm* (with knowledge risk applied) to calculate the error estimates for this category.

$$GE_{mean} = (GE_{worst} - (qfm * k) * (GE_{worst} - GE_{best}))_{mean}$$
$$GE_{std} = (GE_{worst} - (qfm * k) * (GE_{worst} - GE_{best}))_{std}$$

2. Regional field error (RE).

   Virtually all magnetic surveys undergo some type of regional correction during data processing. Typically, a calculated IGRF appropriate to the date of data collection is applied to the total field (F) survey measurements (ideally after the application of a base station diurnal correction). Additionally, some form of regional correction (e.g., using a model, such as MF7) may be applied during the grid leveling and compilation phase. The resulting final compilation grid will then have a regional difference from the true magnetic field that is related to the error in the IGRF and/or another regional model employed.

Again, we make estimates of the best (5 nT mean, 10 nT standard deviation) and worst (100 nT mean, 200 nT standard deviation) possible scenarios for this type of error, *qfr*, and then use our judgment to create a quality factor to select the grid value within that range.

$$RE_{mean} = (RE_{worst} - (qfr * k) * (RE_{worst} - RE_{best}))_{mean}$$
$$RE_{std} = (RE_{worst} - (qfr * k) * (RE_{worst} - RE_{best}))_{std}$$

3. Knowledge factor (k).

For all of the error estimates we "risk" the quality factor using an additional factor to indicate our level of knowledge about the given grid compilation. The knowledge quality factor ranges from 0 (we have no actual knowledge about the compilation grid) to 1 (we created the regional grid ourselves or the grid has very complete metadata documentation).

3.1.2. Overall Error Estimate

The mean (bias), standard deviation (precision), and total error for each of the regional compilation grids are listed in Table 2. These error values are combined from the three sources of error (survey-level noise, grid leveling errors, and regional (IGRF) errors) estimated for each regional compilation grid and introduced above in section 4.1.1. The full spreadsheet showing the individual error source estimates and combination calculations is included as a supporting information to this article.

The overall mean (bias) error (*MEAN*) is calculated by taking the sum of the component means,

$$MEAN = SE_{mean} + GE_{mean} + RE_{mean}$$

Note that we list mean errors as absolute values because there is no way of knowing whether the mean value of a compilation grid is biased toward positive or negative relative to the true magnetic anomaly values.

The overall standard deviation (*STD*), also called precision, around the mean error is calculated from the component deviations using the following formula,

$$STD = SQRT\left(SE_{std}^2 + GE_{std}^2 + RE_{std}^2\right)$$

The total error (*TE*) is defined as follows:

$$TE = SQRT\left(MEAN^2 + STD^2\right)$$

3.2. Trackline Grid Error

The marine grid tiles of the EMAG2 compilation are built from marine cruise survey data in the NCEI data holdings. The individual marine cruises were conducted at various times using different equipment packages (both for navigation and for magnetic data measurement). As a part of our data processing protocol, we created linear trackline segments from the NCEI cruise-level trackline files. The crossing error (difference in measured magnetic field value between two crossing trackline segments where they intersect) for these trackline segments provides information about measurement uncertainty.

For the marine tiles used in EMAG2v3, we calculated the statistics for crossing errors for representative test regions as an estimate of ultimate grid uncertainty (Table 1). In order to complete this analysis, the tile databases were subsampled so that the remaining survey lines had an azimuth $\pm 20^\circ$ from the cardinal directions. This was done to take advantage of the Geosoft Intersections tool, which has issues when crossings are subparallel.

Tie-line leveling, using an orthogonal set of tie-lines to level a main set of generally parallel tracklines, is used to reduce diurnal drift, by shifting individual line levels in traditional dedicated magnetic surveys. Successful tie-line leveling requires that the survey grid be regular and orthogonal. It is also helpful if the datum level of the tie-lines is trustworthy (e.g., the tie-line was flown continuously over a time interval that is short relative to expected diurnal variations) versus that of the main flight lines. Most marine surveys used in this project do not meet criteria (i.e., regular line spacing and orthogonal tie-line crossings) conducive to successful tie-line leveling. We did not employ tie-line leveling for our marine data tiles.

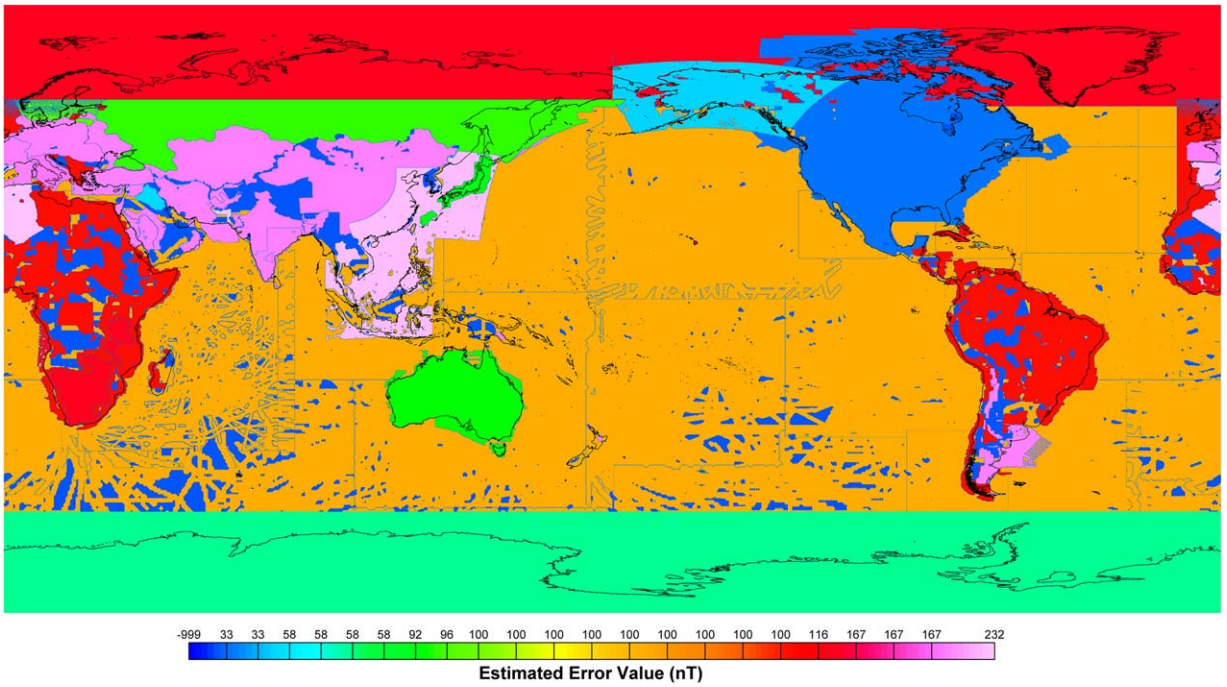

Figure 3. Map of error distribution in EMAG2v3 in nT (Mercator projection). Areas where no trackline or grid data is available are colored with the darkest blue.

For the previous EMAG2 compilation, Maus et al. (2009) estimated the total RMS error, calculated from the mean (bias) error and standard deviation (precision or random error) for the marine trackline data given in the NGDC (now NCEI) holdings as 70 nT. This error was calculated by first subtracting the CM4 model from the survey data wherever total field data were available (otherwise they used available residual data) followed by line leveling to minimize offsets between surveys and finally calculating total survey errors from the crossovers of the entire database. While the line leveling reduced the RMS error from 92 to 70 nT, bias errors persisted in the residual data set. Defining total error as the root-mean-square summation of the bias and random errors, this analysis yielded a global bias error of 65 nT for all the marine trackline surveys in the current NCEI marine trackline system.

Based on our cross-line difference tests (see Table 1) for the current compilation, we feel that the prior error estimate of 70 nT (estimated in Maus et al., 2009) is both too low and implies an unwarranted precision. Estimation of absolute error for the highly complex and varied global marine trackline database is an inherently difficult operation. In detail, the errors and uncertainties vary widely based on a number of factors including data vintage, general lack of independent diurnal variation control, and suboptimal survey geometries, make it difficult to provide precise error determination. The creation of individual marine tile databases for this project allow for the possibility of more complete error analysis in the future.

Our current analysis leads us to the general total error estimate of about 100 nT (the average of the total error for all of the component grids—see Table 1) for the marine regions of the grid. As shown in Table 1, areas with dense line coverage will generally have lower uncertainty relative to areas (particularly in the southern hemisphere) with sparse data coverage. Although out of caution, we only provide the total error of 100 nT in the EMAG2v3 file and associated error map (Figure 3), users interested in the error estimate for a particular tile can find it in Table 1.

4. Results and Analysis

The magnetic anomalies depicted in EMAG2v3 (Figure 1) are caused primarily by the complex distribution of magnetic minerals (most importantly from the iron-bearing magnetite series) in rocks of the crust and upper mantle. At the global scale, the general magnetic anomaly trends and patterns reflect gross tectonic character. For example, the tectonic processes that form oceanic crust result in very different magnetic anomaly patterns than those of continental crust.

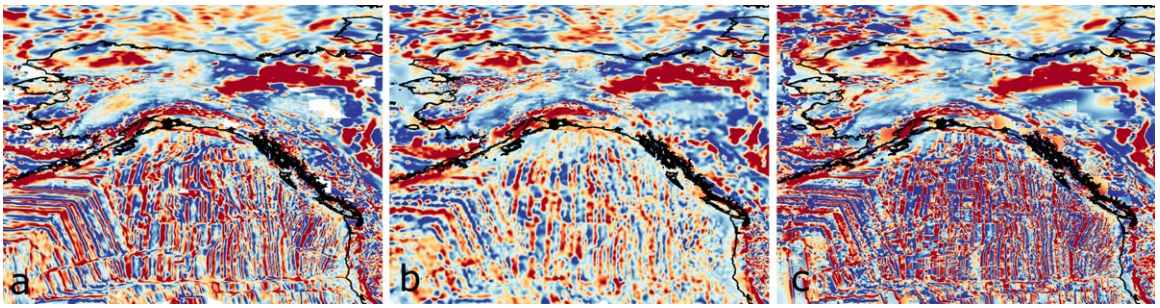

Figure 4. Northeast Pacific magnetic anomalies (a) EMAG2, (b) EMAG2v3, and (c) WDMAM.

The Curie temperature of magnetite (585°C) is an important factor influencing the depth to which magnetic minerals interact with the Earth's field to produce induced magnetic anomalies. In the oceans, the depth to the Curie isotherm will generally increase with ocean-age (and thus with distance from the central ocean ridge). As a result, one expects to see a decrease in magnetic anomaly amplitudes surrounding active mid-ocean ridges.

The most intense crustal magnetic anomalies are found over the old, cold cratonic cores of the continents. The best examples are high-latitude areas with good overall magnetic data coverage, such as central Canada (parts of the Laurentian Shield), Fennoscandia (Fennoscandian Shield), northern Russia (Siberian Craton), and the central cratons of Australia. Portions of the African Shield are evident in EMAG2v3, but regional magnetic data coverage for South America does not do a good job of imaging the South American shields and cratons.

At a more local (but still broad) scale, large-amplitude, circular to oval, zones of high amplitude magnetic highs and lows superimposed on larger wavelength highs correlate with Large Igneous Provinces (LIPs). Well imaged examples (from regions with good magnetic survey coverage) include the High Arctic Large Igneous Province, the Siberian Traps, the Central Atlantic Magmatic Province, and the Deccan Traps (e.g., Oakey & Saltus, 2016).

The magnetic character of oceanic crust is dominated by the induced and remanent magnetic "stripes" that arise from the formation of oceanic crust along mid-ocean ridges (Vine & Matthews, 1963). In EMAG2v3, this distinctive pattern is best seen in high-latitude areas with good marine trackline coverage such as the north Atlantic, northeast Pacific, and some other regions close to major marine ports of call. Low-latitude regions (e.g., within 20° of the equator) have a different magnetic character because of the low inclination angle of the Earth's main magnetic field and the way that affects induced magnetic anomalies (e.g., Blakely, 1995). Figures 4–6 compare three of the global magnetic anomaly compilations, EMAG2 (Maus et al., 2009), EMAG2v3, and the latest WDMAM (Lesur et al., 2016). The intensity of the anomalies for EMAG2v3 is significantly reduced from the other two models, and it does not have long continuous lines of positive and negative anomalies, but rather demonstrates potential heterogeneity and complexity of the evolution along oceanic spreading ridges. Without the a priori information, we are still able to retrieve the large-scale structures. Also in Figure 4 is the updated precompiled continental grid for Alaska, where more high-energy

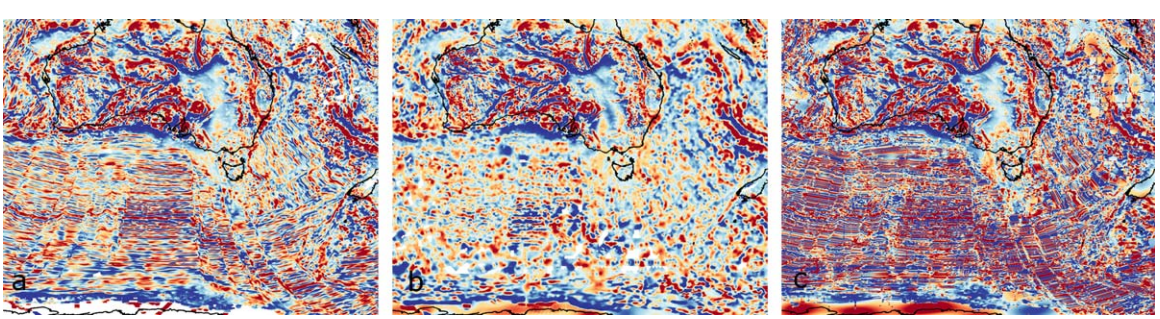

Figure 5. Southern Ocean magnetic anomalies (a) EMAG2, (b) EMAG2v3, and (c) WDMAM.

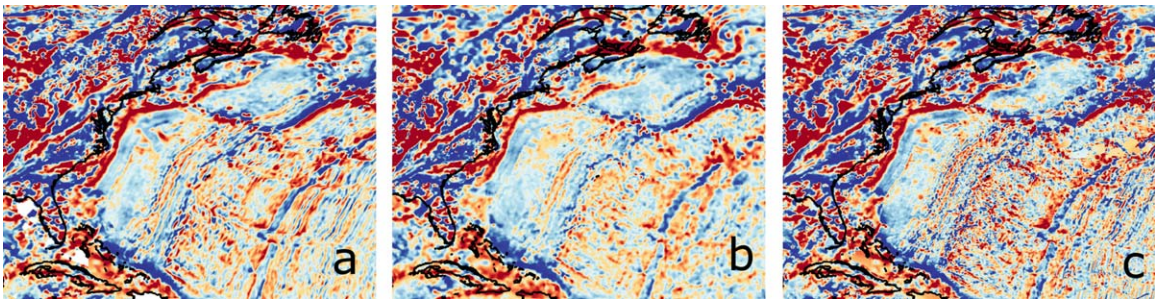

Figure 6. Northwest Atlantic magnetic anomalies (a) EMAG2, (b) EMAG2v3, and (c) WDMAM.

anomalies are visible. For EMAG2v3, smooth grid margins were a priority, not solely boundaries between continental and oceanic regions, but within continents as well. Also by further utilizing airborne data, we were able to fill in some continental gaps that exist in EMAG2.

As discussed above, a significant way that EMAG2v3 differs from EMAG2 and the latest WDMAM is that a priori information on oceanic magnetic anomalies were not used. As a result, many areas with sparse marine trackline coverage do not show the diagnostic oceanic stripe character. For example, the south Pacific adjacent to Antarctica is devoid of diagnostic oceanic stripes. In the area shown in Figure 5, between the south coast of Australia and Antarctica, we can see significant differences between the three grids. This is an area with low data density within the GEODAS database, so without using a priori knowledge of the ocean floor structure there is not enough data to detect the complex ocean striping pattern, but that is not to say that this pattern is not present. When studying and interpreting oceanic magnetic anomalies we recommend that users consult and compare a number of global models, and, in particular, that they examine the differences between EMAG2 and EMAG2v3. In Figure 5, when looking at the continental Antarctica, the differences between the continental data processing also varies between the models. EMAG2 does not utilize the Antarctic Digital Magnetic Anomaly Project anomaly grid, but the two other models do. There are subtle differences between the two grids, which can be attributed to the fact that the long-wavelength anomaly features are directly obtained from MF7, not MF6 (utilized by EMAG2).

It is also instructive to compare a priori ocean-age based grids to EMAG2v3 in areas of good marine trackline coverage, such as the north Atlantic shown in Figure 6. In this area, the intensities of the anomalies are more consistent across the models, and the large-scale structures are in good agreement. In a number of cases, it is interesting to note that the EMAG2v3 anomalies show significantly less regularity than predicted by the idealized ocean-age models. In many cases this may indicate that the structure and mineral composition of the oceanic crust is more complex than the models predict.

Another feature of the EMAG2v3 is that we also deliver a grid where the anomalies are reported at sea level (Figure 2). This version is especially useful for evaluating deep ocean structures, where the observations are made multiple kilometers from the source rock to begin with. It is also useful for evaluating continental margins where gradients can be higher (especially vertical derivatives) that can expose further information about the local lithology.

Table 3 shows standard deviations between the 4 km altitude version of the EMAG2v3, EMAG2, and the WDMAM (downward continued from 5 to 4 km) when compared to the trackline anomalies. These anomalies are the same data used in the calculation of the final grid, but for this analysis the tracks were independently upward continued to 4km.

For most of the tiles, the EMAG2v3 has significantly lower standard deviations than the other two grids. The primary reason for this is that this is the same data that went into the construction of the EMAG2v3 and thus will naturally be in greater agreement. Another reason is that by forcing the grid to match some a priori information, the WDMAM and EMAG2 (in different ways) impose some constraints on grid values that will eventually lead to larger residuals.

This analysis shows that areas with high data density, such as the North Atlantic tiles, the EMAG2v3 performs very well, as well as the grids which utilize a priori information. In regions of poor data quality and

Table 3
Standard Deviation (nT) Between Recalculated Trackline Anomalies and EMAG2v3, EMAG2, and WDMAM at 4 km Altitude for Each Oceanic Tile

Tile	EMAG2v3	EMAG2	WDMAM (4km)
Tasmania/South Australia	46.4	64.4	102.9
Southwest Atlantic	98.1	120.3	162.7
Southeast Pacific	51.0	63.1	103.2
South Pacific	125.1	135.1	165.1
Southern Ocean	78.0	253.0	259.6
Northwest Pacific	55.1	76.8	112.3
North Pacific	84.0	135.2	162.7
North Atlantic 5	82.4	89.0	133.5
North Atlantic 4	83.5	97.1	131.8
North Atlantic 3	37.5	49.0	64.2
North Atlantic 2	70.64	94.6	114.3
North Atlantic 1	50.1	67.6	92.5
Mediterranean	34.4	39.7	54.8
Indian Ocean	43.9	74.3	92.5
Cape of Good Hope/Southeast Atlantic	57.8	217.8	232.8
Tierra del Fuego/Southeast Pacific	94.2	108.9	136.7
Central Atlantic	49.9	71.5	85.5
Caribbean/Gulf of Mexico	42.8	50.9	67.2
Baja California/Eastern Pacific	37.4	59.6	99.3
Arabian Ocean Shipborne	50.3	60.9	107.3
Arabian Ocean Airborne	84.9	61.1	102.3

coverage, such as the Southwest Atlantic and South Pacific tiles, all three grids struggle to accurately represent the magnetic signatures of the ocean basins. Because there is less data to constrain the grids, the a priori information has a stronger impact on EMAG2 and WDMAM in those areas. The smaller residuals for these two grids in some of these areas (e.g., Southwest Atlantic) versus others (e.g., Southern Ocean) suggest that the a priori information is closer to reality in the former. In areas where a priori information is in good agreement with the available data, it might even act like a regularization that stabilizes the gridding process; hence it could be that EMAG2 (and to lesser extent WDMAM) provide superior predictive capability than EMAG2v3 in some of these areas, However, we can see from this analysis, especially in the southern hemisphere, that the a priori information used to construct other grids may not be as accurate as we expect.

5. Conclusions

With the construction of the EMAG2v3 grid, we have demonstrated that it is possible to create a global scale map of magnetic anomalies at 2 arc min resolution without using a priori information about the age of the ocean floor and plate motions. The obtained grid substantially differs from EMAG2 and the latest WDMAM over oceanic areas, while being closer to the data, by a large margin in some areas. This suggests that some of the a priori information used in EMAG2 and WDMAM might need to be revised in some areas. In areas where the data density is too low to recover any expected anomaly pattern, it could be advantageous to use grids including some a priori information, provided residuals between such grids and trackline data are not too large. Whatever the use of the grid, it is important to keep in mind the limitations imposed by the lack of data in many oceanic areas.

EMAG2v3 also reports gridded anomalies at sea level as an additional grid product. Though the WDMAM reports marine data at sea level, this is done in the same grid as the 5 km altitude continental regions, which could cause some confusion. At sea level, most observations are already multiple kilometers away from the source rock. Further upward continuation attenuates these details, and the inclusion of a priori information can smear or obfuscate these details. It is possible that with this method of grid construction, further insight into the complexity of plate boundary evolution can be understood in more detail.

Over 50 million new marine and airborne magnetic observations have been added to GEODAS in recent years. In this time, new regional compilations have also been added to the ever-increasing archive of NCEI.

Acknowledgments
We would like to thank every scientist, academic institution, international governmental body, or private contractor who contributed data to the Geophysical Data System at NOAA NCEI. Trackline data provided by Scripps Institution of Oceanography, Lamont-Doherty Geological Observatory, Geological Survey of Japan, Hydrographic Department of Japan, University of Hawaii, IFREMER, US National Oceanic and Atmospheric Administration, United States Geologic Survey, Woods Hole Oceanographic Institution, US Navy Naval Oceanographic Office, Ocean Drilling Program at Texas A and M, Bundesanstalt für Geowissenschaften und Rohstoffe, Bedford Institute of Oceanography, University of Texas Institute for Geophysics, Institute of Oceanographic Sciences UK, CNEXO, Oregon State University, Bureau of Mineral Resources Australia, Geophysics Division DSIR New Zealand, US Navy NORDA, Texas A and M University, Natural Environment Research Council UK, BNDO, GNS Science New Zealand, University of Tokyo, Geological Survey of Canada, Australian Geological Survey Organisation, GEOMER Data Bank ORSTOM Noumea, Kobe University, Canadian Hydrographic Service, Mobil, Hydrographic Department MSA, Institute of Marine Geology/ Geophysics USSR, Oregon State University, United Kingdom Hydrographic Office, University of Rhode Island, Geological Survey of Ireland, GEOMAR Germany, NIWA New Zealand, Russian Academy of Science, South African Data Centre for Oceanography, University of Witwatersrand, Royal Netherlands Navy Hydrographic Service, Chiba University, Land Information New Zealand, Southampton Oceanography Centre, University of Cape Town, University of the Ryukyus, Bundesamt Seeschiffahrt Hydrographie, GuangZhou Marine Geological Survey MGMR, National Institute of Polar Research Japan, National Science Foundation, ORSTOM, Rice University, South African Geological Survey, University of Alabama, University of Cape Town, University of Texas at Austin, University of Rhode Island, BP Shell Todd, British Antarctic Survey, British Oceanographic Data Centre, Diamond Shamrock Petroleum, Far East Scientific Center, First Institute of Oceanography, SOA, Hamilton College, Institut de Physique du Globe de Paris, Jet Propulsion Laboratory, National Research Institute Oceanology South Africa, Petrocorp, Stewart Petroleum, Universite Francaise Pacifique Tahiti, University of California at San Diego, Project Magnet, Antarctic Digital

These new data additions have helped us cover areas where no data had previously existed. We also relied on an improved satellite-based lithospheric field model, MF7, to generate the long wavelengths of the grid.

Important other aspects of the new grid are that it comes with error estimates, that it is fully traceable to source data and that it can quickly be updated. Errors were derived from a comprehensive analysis of continental grids and oceanic trackline data. Although it is hard to recover accurate error information for some grids, especially older ones, we devised a method to estimate what we think are reasonable values for all grids. The model construction taking place as discrete tiles allows for future updates to the EMAG2 to be released more frequently as new trackline data and regional compilations become available.

Further insight into the heterogeneous nature of the error distribution of the source data for the EMAG2v3 shows that there are still many areas of the world where we are reliant on older, low resolution data, and where source data are not available to apply modern gridding techniques to possibly improve the final products. In many of the more remote sections of the ocean which have not been revisited by research vessels in many decades, this may be the only ground truth data available. By evaluating this distribution, we hope to convey to the user where we have the greatest confidence in our observations. This has the added benefit of signifying to the greater scientific community where effort should be made to focus future data collection missions.

The primary focus for future updates is always data collection. Acquiring data can be done as they come off of ships, as primary investigators publish their work on the data, or as data are digitized and rescued. Improving the error analysis and reporting is underway and will be made available with future updates. Smaller, higher resolution grids are also possible to generate using our processing method in areas where data density is sufficient.

References

Backus, G. E. (1970). Non-uniqueness of the external geomagnetic field determined by surface intensity measurements. *Journal Geophysical Research*, *75*(31), 6339–6341.

Bankey, V., Cuevas, A., Daniels, D., Finn, C. A., Hernandez, I., Hill, P., . . . Ravat, D. (2002). *Digital data grids for the magnetic anomaly map of North America* (U.S. Geol. Surv. Open File Rep. 02–414). Reston, VA: U.S. Geological Survey.

Blakely, R. J. (1995). *Potential theory in gravity and magnetic applications*. Cambridge, UK: Cambridge University Press.

Claus, B., & Bachmayer, R. (2017). A parameterized geometric magnetic field calibration method for vehicles with moving masses with applications to underwater gliders. *Journal of Field Robotics*, *34*(1), 209–223. https://doi.org/10.1002/rob.21660

Dickson, W., Schiefelbein, C. F., Odegard, M. E., & Zumberge, J. E. (2016). Petroleum systems asymmetry across the South Atlantic Equatorial Margins, *Geological Society Special Publications*, 431(1), 219–233. https://doi.org/10.1144/SP431.13

Dyment, J., Choi, Y., Hamoudi, M., Lesur, V., & Thébault, E. (2015). Global equivalent magnetization of the oceanic lithosphere. *Earth Planetary Science Letters*, *430*, 54–65. https://doi.org/10.1016/j.epsl.2015.08.002

Finlay, C. C., Olsen, N., & Toeffner-Clausen, L. (2015). DTU candidate field models for IGRF-12 and the CHAOS-5 geomagnetic field model. *Earth Planets Space*, *67*, 114. https://doi.org/10.1186/s40623-015-0274-3

Gaina, C., Werner, S., Saltus, R., Maus, S., & the CAMP-GM group. (2011). Circum-Arctic mapping project: New magnetic and gravity anomaly maps of the arctic. In A. M. Spencer, D. Gautier, A. Stoupakova, A. Embry, & K. Sørensen (Eds.), *Geological Society, London, Memoirs Arctic petroleum geology* (Vol. 35). London, UK: Geological Society of London. https://doi.org/10.1144/M35.3

Geological Survey of Japan and Coordinating for Coastal and Offshore Geoscience Programs in East and Southeast Asia (CCOP) (2002). *Magnetic anomaly map of East Asia* (2nd ed., scale 1:4,000,000) [CD-ROM], *Digital Geoscience Map*. Tokyo, Japan: Geological Survey Japan, AIST

Goovaerts, P. (1997). *Geostatistics for natural resources evaluation*. New York, NY: Oxford University Press.

Hamoudi, M., Thébault, E., Lesur, V., & Mandea, M. (2007). GeoForschungsZentrum Anomaly Magnetic Map (GAMMA): A candidate model for the World Digital Magnetic Anomaly Map. *Geochemistry, Geophysics, Geosystems*, *8*, Q06023. https://doi.org/10.1029/2007GC001638

Hinze, W. J., & Zietz, I. (1985). The composite magnetic-anomaly map of the conterminous United States. In W. J. Hinze (Ed.), *The utility of regional gravity and magnetic anomaly maps* (pp. 1–24). Tulsa, OK: Society of Exploration Geophysicists.

Jaeger, J. M., Gulick, S. P. S., LeVay, L. J., Asahi, H., Bahlburg, H., Belanger, C. L., . . . Worthington, L. L. (2014). Site U1417. In J. M. Jaeger et al. (Eds.), *Proceedings of the international ocean drilling program* (341 p.). College Station, TX: Integrated Ocean Drilling Program. https://doi.org/10.2204/iodp.proc.341.103.2014

Korhonen, J. V., Aaro, S., All, T., Nevanlinna, H., Skilbrei, J. R., Saavuori, H., . . . Koinstinen, T. (2002). Magnetic anomaly map of the Fennoscandian Shield: DGRF-65 anomaly of total field. Anomaly continued upwards to 500 m above ground, scale 1:2 000 000. Espoo: Geological Survey of Finland, Trondheim: Geological Survey of Norway, Uppsala: Geological Survey of Sweden, Moscow: Ministry of Natural Resources of Russia.

Korhonen, J. V., Fairhead, J. D., Hamoudi, M., Hemant, K., Lesur, V., Mandea, M., . . . Thebault, E. (2007). *Magnetic anomaly map of the world* (1st ed., scale 1:50,000,000). Helsinki, Finland: Geological Survey of Finland.

Langel, R. A., & Hinze, W. J. (1998). *The magnetic field of the Earth's lithosphere: The satellite perspective*. Cambridge, UK: Cambridge University Press.

Lesur, V., Hamoudi, M., Choi, Y., Dyment, J., & Thébault, E. (2016). Building the second version of the World Digital Magnetic Anomaly Map (WDMAM). *Earth Planets Space*, *68*, 27. https://doi.org/10.1186/s40623-016-0404-6

Lowes, F. J. (1966). Mean-square values on sphere of spherical harmonic vector fields. *Journal Geophysical Research*, *71*(8), 2179.

Magnetic Anomaly Project, DTU IceGrav. Regional compilation grids provided by Aeromagnetics of Arabia, India and the Middle East project, Antarctic Digital Magnetic Anomaly project, USGS, Canadian International Development Agency, Southern African Development Community, Institut de Physique du Globe de Paris, Coordinating Committee for Geoscience Programs in East and Southeast Asia, Getech, Juha Korhonen, Mike Purucker, Mark Pilkington, Rick Saltus. The EMAG2v3 is available at https://www.ngdc.noaa.gov/geomag/emag2.html or https://doi.org/10.7289/V5H70CVX.

Matzka, J., Rasmussen, T. M., Olesen, A. V., Nielsen, J. E., Forsberg, R., Olsen, N., . . . Verhoef, J. (2010). A new aeromagnetic survey of the North Pole and the Arctic Ocean north of Greenland and Ellesmere Island. *Earth Planets Space*, *62*, 829–832. https://doi.org/10.5047/eps.2010.07.002

Maus, S. (2010). An ellipsoidal harmonic representation of Earth's lithospheric magnetic field to degree and order 720. *Geochemistry, Geophysics, Geosystems*, *11*, Q06015. https://doi.org/10.1029/2010GC003026

Maus, S., Barckhausen, U., Berkenbosch, H., Bournas, N., Brozena, J., Childers, V., . . .Tontini, F. C. (2009). EMAG2: A 2-arc min resolution Earth Magnetic Anomaly Grid compiled from satellite, airborne, and marine magnetic measurements. *Geochemistry, Geophysics, Geosystems*, *10*, Q08005. https://doi.org/10.1029/2009GC002471

Maus, S., Lühr, H., Rother, M., Hemant, K., Balasis, G., Ritter, P., & Stolle, C. (2007a). Fifth-generation lithospheric magnetic field model from CHAMP satellite measurements. *Geochemistry, Geophysics, Geosystems*, *8*, Q05013. https://doi.org/10.1029/2006GC001521

Maus, S., Nair, M. C., Poedjono, B., Okewunmi, S., Fairhead, J. D., Barckhausen, U., . . . Matzka, J. (2012, 6–8 March). High definition geomagnetic models: A new perspective for improved wellbore positioning. In *IADC/SPE drilling conference and exhibition*, San Diego, CA. https://doi.org/10.2118/151436-MS

Maus, S., Sazonova, T., Hemant, K., Fairhead, J. D., & Ravat, D. (2007b). National Geophysical Data Center candidate for the World Digital Magnetic Anomaly Map. *Geochemistry, Geophysics, Geosystems*, *8*, Q06017. https://doi.org/10.1029/2007GC001643

Maus, S., Yin, F., Lühr, H., Manoj, C., Rother, M., Rauberg, J., . . . Müller, R. D. (2008). Resolution of direction of oceanic magnetic lineations by the sixth-generation lithospheric magnetic field model from CHAMP satellite magnetic measurements. *Geochemistry, Geophysics, Geosystems*, *9*, Q07021. https://doi.org/10.1029/2008GC001949

Max, M. D., Ghidella, H., Kovaks, L., Paterlini, M., & Valladares, J. A. (1999). Geology of the Argentine continental shelf and margin from aeromagnetic survey. *Marine and Petroleum Geology*, *9*, 590–601.

Milligan, P. R., Franklin, R., & Ravat, D. (2004). A new generation of Magnetic Anomaly Grid Database of Australia (MAGDA) - use of independent data increases the accuracy of long wavelength components of continental-scale merges. *Preview*, *113*, 25–29.

Muüller, R. D., Qin, X., Sandwell, D. T., Dutkiewicz, A., Williams, S. E., Flament, N., . . . Seton, M. (2016). The GPlates Portal: Cloud-based interactive 3D visualization of global geophysical and geological data in a web Browser. *PLoS ONE*, *11*(3), e0150883. https://doi.org/10.1371/journal.pone.0150883

Müller, R. D., Sdrolias, M., Gaina, C., & Roest, W. R. (2008). Age, spreading rates, and spreading asymmetry of the world's ocean crust. *Geochemistry, Geophysics, Geosystems*, *9*, Q04006. https://doi.org/10.1029/2007GC001743

Nakatsuka, T., Okuma, S., Makino, M., & Morijiri, R. (2005). *Aeromagnetic database of Japan* [2 CD-ROM discs]. *Digital Geoscience Maps, P-6*, Tokyo, Japan: Geological Survey Japan, AIST.

Oakey, G. N., & Saltus, R. W. (2016). Geophysical analysis of the Alpha–Mendeleev ridge complex: Characterization of the High Arctic Large Igneous Province. *Tectonophysics*, *691*(Part A), 65–84. https://doi.org/10.1016/j.tecto.2016.08.005

Rajaram, M., Anand, S. P., & Balakrishna, T. S. (2006). Composite magnetic anomaly map of India and its contiguous regions. *Geological Society of India*, *68*(4), 569–576.

Reigber, C., Lühr, H., & Schwintzer, P. (2002). CHAMP mission status. *Advances in Space Research*, *30*(2), 129–134.

Sabaka, T. J., Olsen, N., & Purucker, M. E. (2004). Extending comprehensive models of the Earth's magnetic field with Ørsted and CHAMP data. *Geophysical Journal International*, *159*, 521–547. https://doi.org/10.1111/j.1365-246X.2004.02421.x

Saltus, R. W. (2007). Regional magnetic survey compilations—Current issues. *Gondwana Research*, *11*(4), 580–581.

Schlindwein, V., & Schmid, F. (2016). Mid-ocean-ridge seismicity reveals extreme types of ocean lithosphere. *Nature*, *535*, 276–279. https://doi.org/10.1038/nature18277

Seton, M., Müller, R. D., Zahirovic, S., Gaina, C., Torsvik, T., . . .Chandler, M. (2012). Global continental and ocean basin reconstructions since 200Ma. *Earth-Science Reviews*, *113*(3–4), 212–270. https://doi.org/10.1016/j.earscirev.2012.03.002

Snieder, R., & Trampert, J. (1999). Inverse problems in geophysics. In A. Wirgin (Ed.), *Wavefield inversion* (pp. 119–190). New York, NY: Springer.

Socias, I., & Mezcua, J. (1996). *Levantamiento aeromagnetico del archipielago canario* (Publ. Tec., 35, 28 p.). Madrid, Spain: Instituto Geografico Nacional.

Socias, I., Mezcua, J., Lynam, J., & Del Potro, R. (1991). Interpretation of an aeromagnetic survey of the Spanish mainland. *Earth and Planetary Science Letters*, *105*, 55–64.

Stern, D. P., & Bredekamp, J. H. (1975). Error enhancement in geomagnetic models derived from scalar data. *Journal of Geophysical Research*, *80*(13), 1776–1782.

Sweeney, R. E., Abraham, J. D., Anderson, E. D., Drenth, B. J., Finn, C. A., . . . Kucks, R. P. (2007). *Aeromagnetic survey in Afghanistan: A website for distribution* (U.S. Geol. Surv. Open File Rep. 2007-1247). Reston, VA: United States Geological Survey.

Thébault, E., Finlay, C. C., Beggan, C., Alken, P., Aubert, J., Barrois, O., . . . Zvereva, T. (2015). International geomagnetic reference field: The twelfth generation. *Earth Planets Space*, *67*(7), 114. https://doi.org/10.1186/s40623-015-0228-9

Thébault, E., Hemant, K., Hulot, G., & Olsen, N. (2009). On the geographical distribution of induced time-varying crustal magnetic fields. *Geophysical Research Letters*, *36* (1), 1–5.

Vérard, C., Flores, K., & Stampfli, G. (2012). Geodynamic reconstructions of the South America–Antarctica plate system. *Journal of Geodynamics*, *53*, 43–60. https://doi.org/10.1016/j.jog.2011.07.007

Verhoef, J., Roest, W., Macnab, R., & Arkani-Hamed, J., & Members of the Project (1996). *A compilation of magnetic observations from the Arctic and North Atlantic Oceans and adjacent land areas* [CD-ROM data release] (Open File 3125a, 577 p.). Ottawa, Canada: Geological Survey of Canada. https://doi.org/10.4095/207789

Vine, F. J., & Matthews, D. H. (1963). Magnetic anomalies over oceanic ridges. *Nature*, *4897*, 947–949.

Webb, L. E., Johnson, C. L., & Minjin, C. (2010). Late Triassic sinistral shear in the East Gobi Fault Zone, Mongolia. *Tectonophysics*, *495*(3–4), 246–255. https://doi.org/10.1016/j.tecto.2010.09.033

Williams, S. E., Whittaker, J. M., & Müller, R. D. (2011). Full-fit, palinspastic reconstruction of the conjugate Australian-Antarctic margins. *Tectonics*, *30*, TC6012. https://doi.org/10.1029/2011TC002912

Wonik, T., Trippler, K., Geipel, H., Greinwald, S., & Pashkevitch, I. (2001). Magnetic anomaly map for Northern, Western, and Eastern Europe. *Terra Nova*, *13*, 203–213.

Zheng, H., Wang, H., Wu, L., Chai, H., & Wang, Y. (2013). Simulation research on gravity-geomagnetism combined aided underwater navigation. *Journal of Navigation*, *66*, 83–98. https://doi.org/10.1017/S0373463312000343